Molecular Cell

Article

Structural insights into DNMT5-mediated ATP-dependent high-fidelity epigenome maintenance

Graphical abstract

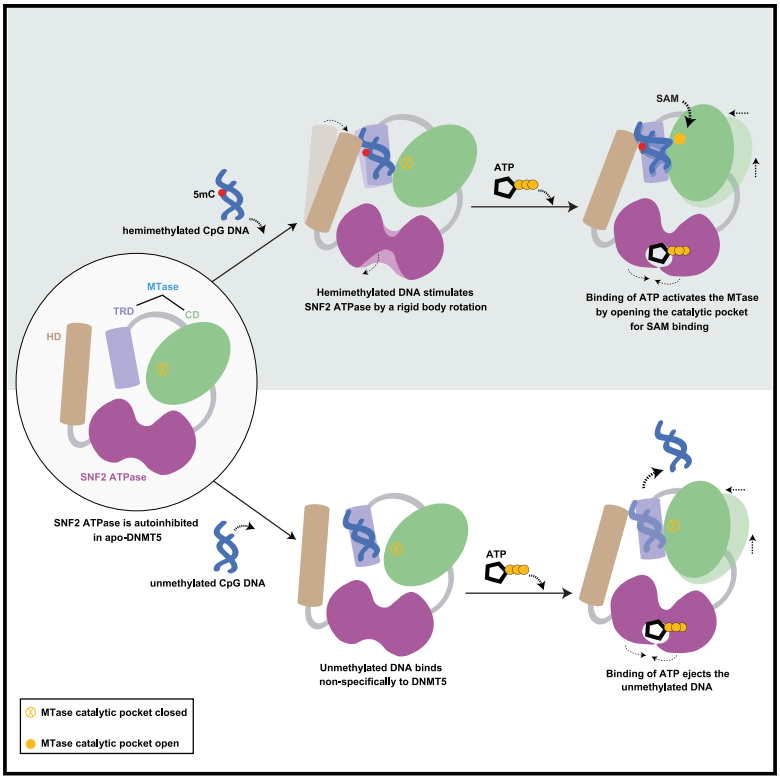

Highlights

- Structures of DNMT5 reveal the mechanism of ATP-dependent DNA methylation
- Hemimethylated CpG recognition triggers partial base flipping of the target cytosine
- Hemimethylated DNA induces rigid body rotation to activate the SNF2 ATPase domain
- SNF2 ATPase regulates the MTase activity to achieve ultrahigh specificity

Authors

Juncheng Wang, Sandra Catania, Chongyuan Wang, M. Jason de la Cruz, Beiduo Rao, Hiten D. Madhani, Dinshaw J. Patel

Correspondence

wangj1@mskcc.org (J.W.), hitenmadhani@gmail.com (H.D.M.), pateld@mskcc.org (D.J.P.)

In brief

With an elegant set of three cryo-EM structures, Wang et al. reveal the mechanism of ATP-dependent DNA methylation in the DNA methyltransferase DNMT5. SNF2 ATPase regulates the methyltransferase activity to achieve ultrahigh specificity, which is critical for epigenome maintenance over million-year timescales in the human pathogenic fungus *Cryptococcus neoformans*.

Wang et al., 2022, Molecular Cell *82*, 1186–1198
March 17, 2022
https://doi.org/10.1016/j.molcel.2022.01.028

CellPress

CellPress
OPEN ACCESS

Molecular Cell

Article

Structural insights into DNMT5-mediated ATP-dependent high-fidelity epigenome maintenance

Juncheng Wang,[1,4,*] Sandra Catania,[2,4] Chongyuan Wang,[1] M. Jason de la Cruz,[1] Beiduo Rao,[2] Hiten D. Madhani,[2,3,*] and Dinshaw J. Patel[1,5,*]

[1]Structural Biology Program, Memorial Sloan Kettering Cancer Center, New York, NY 10065, USA
[2]Department of Biochemistry and Biophysics, University of California, San Francisco, San Francisco, CA 94158, USA
[3]Chan Zuckerberg Biohub, San Francisco, CA 94158, USA
[4]These authors contributed equally
[5]Lead contact
*Correspondence: wangj1@mskcc.org (J.W.), hitenmadhani@gmail.com (H.D.M.), pateld@mskcc.org (D.J.P.)
https://doi.org/10.1016/j.molcel.2022.01.028

SUMMARY

Epigenetic evolution occurs over million-year timescales in *Cryptococcus neoformans* and is mediated by DNMT5, the first maintenance type cytosine methyltransferase identified in the fungal or protist kingdoms, the first dependent on adenosine triphosphate (ATP), and the most hemimethyl-DNA-specific enzyme known. To understand these novel properties, we solved cryo-EM structures of *Cn*DNMT5 in three states. These studies reveal an elaborate allosteric cascade in which hemimethylated DNA binding first activates the SNF2 ATPase domain by a large rigid body rotation while the target cytosine partially flips out of the DNA duplex. ATP binding then triggers striking structural reconfigurations of the methyltransferase catalytic pocket to enable cofactor binding, completion of base flipping, and catalysis. Bound unmethylated DNA does not open the catalytic pocket and is instead ejected upon ATP binding, driving high fidelity. This unprecedented chaperone-like, enzyme-remodeling role of the SNF2 ATPase domain illuminates how energy is used to enable faithful epigenetic memory.

INTRODUCTION

Maintenance methylation of hemimethylated CpG sites produced by DNA replication is the key to faithful epigenetic inheritance of genomic methylation patterns (Hashimoto et al., 2008). The process is mediated by maintenance DNA methyltransferases (DNMTs) (DNMT1 in animals and MET1 in plants) that recognize hemimethylated DNA (hmDNA) produced by DNA replication. There is almost nothing known about such processes in the two other eukaryotic kingdoms, namely Fungi and Protista, which harbor millions of species. The fungal epigenetic inheritance of DNA methylation patterns was demonstrated in the 1990s in the ascomycete *Ascobolus immersus* (Rossignol and Faugeron, 1995), although the maintenance enzyme responsible was never identified. We recently demonstrated that DNMT5, a DNMT required for CpG methylation in the human pathogenic basidiomycete fungus *Cryptococcus neoformans* (Huff and Zilberman, 2014), is a maintenance enzyme, the first cytosine DNMT to be characterized biochemically in the kingdom Fungi or Protista (Catania et al., 2020; Dumesic et al., 2020). DNMT5 is required for full virulence of *C. neoformans*, indicating an important function (Liu et al., 2008) and making it a potential drug target to inhibit infection (Huff and Zilberman, 2014). Amazingly, *C. neoformans* does not harbor a *de novo* enzyme because the gene for the *de novo* enzyme was lost in an ancestor that lived at least 50 million years (Catania et al., 2020). Methylation is maintained by an epigenetic evolution mechanism that involves replication of methylation patterns by DNMT5, rare epimutations, and natural selection (Catania et al., 2020). Biochemically, DNMT5 is unusual, in that it harbors an SNF2 ATPase domain and requires ATP for DNA methylation (Catania et al., 2020; Dumesic et al., 2020). Moreover, it displays absolute specificity for hmDNA *in vitro* (Dumesic et al., 2020), much greater than mammalian DNMT1, which shows considerable methyltransferase (MTase) activity on unmethylated DNA (umDNA) *in vitro* (Pradhan et al., 1997, 1999; Tollefsbol and Hutchison, 1997) and even *in vivo* (Arand et al., 2012; Biniszkiewicz et al., 2002; Li et al., 2018; Wang et al., 2020).

To understand the mechanisms underlying the ATP dependence and exquisite specificity, we solved cryo-EM structures of DNMT5 in the apo state, in a binary complex with hemimethylated DNA, and a quaternary complex with added nonhydrolyzable ATP analog, AMP-PNP, and S-adenosylmethionine (SAM) reaction product, S-adenosylhomocysteine (SAH). These structures together with biochemical assays reveal a remarkable cascade, in which hmDNA recognition triggers partial base flipping of the target cytosine that is accompanied by a dramatic allosteric movement in the ATPase domain. This is then followed by nucleotide binding by the ATPase domain, which leads to catalytic loop insertion and the completion of substrate base flipping together with restructuring of the catalytic pocket to enable cofactor binding. In addition, ATP binding also licenses ejection of nonspecifically bound umDNA. Overall, these studies illustrate

CellPress
OPEN ACCESS

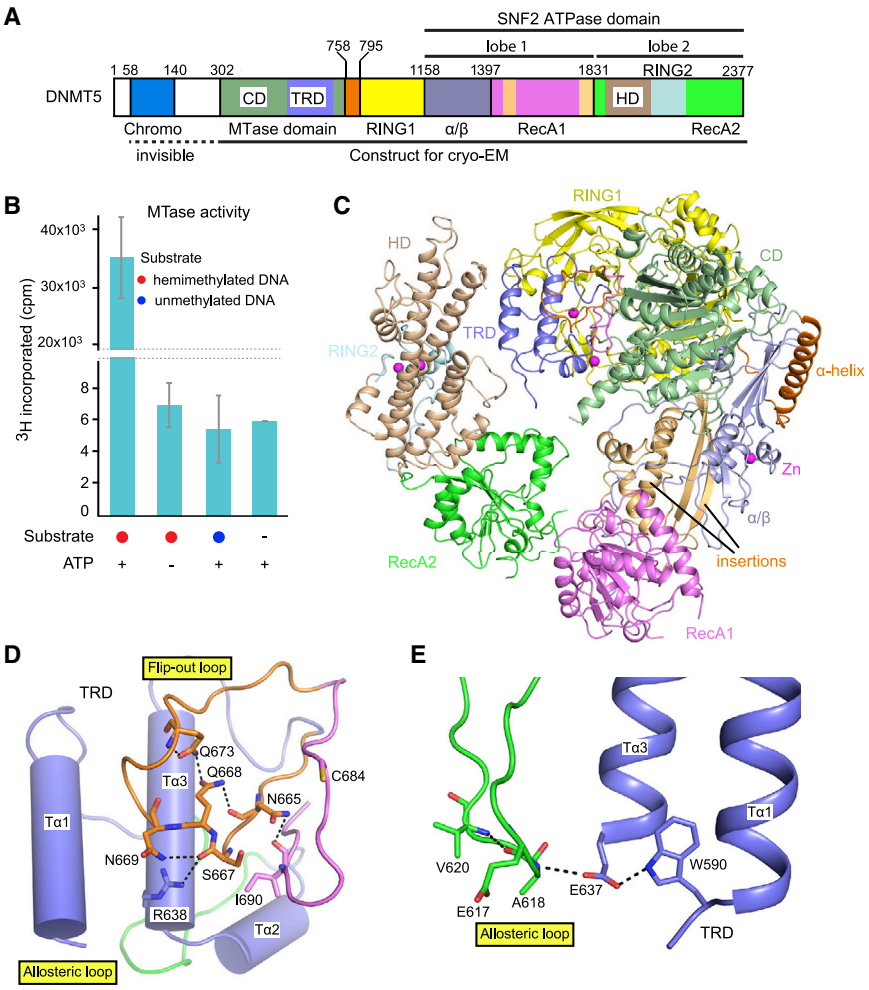

Figure 1. Cryo-EM structure of DNMT5 in the apo state

(A) Color-coded domain architecture and numbering of DNMT5.

(B) MTase activity of DNMT5 on umDNA and hmDNA substrates at the 4-h time point. Error bars represent SD; n = 4.

(C) Ribbon representation of the cryo-EM structure of DNMT5 in the apo state.

(D) The relative alignments of flip out and allosteric loops in the TRD of DNMT5.

(E) A hydrogen-bond network locks the allosteric loop through interaction with the TRD.

See also Figures S1 and S2.

a fundamentally novel signal transduction role for an SNF2 ATPase in an allosteric cascade that supports the remarkable specificity of DNMT5 for hmDNA, a property that is likely critical for epigenome maintenance over million-year timescales.

RESULTS

Overall structure of DNMT5

We expressed near full-length DNMT5 (Figure 1A) including all its structured domains (residues 58 to 2,377) in insect cells. This truncated protein displays remarkable specificity for hmDNA like full-length DNMT5, with no detectable MTase activity on umDNA or on hmDNA in the absence of ATP (Figure 1B). A 36 base pair (bp) DNA containing a single hemimethylated CpG site (Figure 2A) was incubated with DNMT5 supplemented with AMP-PNP and SAH. It was then subjected to gel filtration purification and used for single-particle cryo-EM studies.

We obtained two structures through masked 3D classification with partial signal subtraction (Bai et al., 2015) (Figure S1A), one of which is DNMT5 alone (apo-DNMT5) at 3.3 Å resolution (Figures 1C, S1B, and S1C; Table 1) and the second composed of DNMT5 and hmDNA (binary complex) at 3.1 Å resolution (Figures 2B, S1B, and S1D; Table 1). Side-chain densities of most residues in the binary complex map were clearly resolved, allowing *de novo* model building (Figure S2A). The apo-DNMT5 structure was solved based on the binary complex model (Figure S2B). The N-terminal chromodomain lacks clear density in both the apo and binary complex maps, reflecting its flexible orientation relative to the other domains. Densities of AMP-PNP and SAH are absent in both maps, suggesting dissociation during gel filtration purification.

DNMT5 folds into a compact structure with a ring-like topology (Figure 1C). The MTase domain is folded into two subdomains, labeled catalytic domain (CD) and target recognition domain (TRD). The TRD consists of three α-helices and two loops, designated as the flip out and allosteric loops (Figure 1D). The side chain of Q668 is stabilized by a hydrogen-bond network with Q673 and N665, whereas S667 interacts through hydrogen bonds with N669 and R638 (Figure 1D). On the back of the TRD, the allosteric loop is locked in place by two α-helices (Tα1 and Tα3) through a hydrogen-bond network involving A618, E637, and W590 (Figure 1E).

A long rigid α-helix connects the CD and the first RING zinc-finger domain (RING1). The ATPase domain can be delineated into two lobes (lobe 1 and lobe 2). Lobe 1 contains an α/β region and the first RecA-like domain (RecA1) (Figure 1C). N- and C-terminal insertions of RecA1 make close contacts with the CD and contribute to the extension of the β-sheet in the α/β region (Figure S2C). Lobe 2 consists of the second RecA-like domain (RecA2) and an inserted region including an α-helical domain (HD) and the second RING zinc-finger domain (RING2) (Figures 1A and 1C). The MTase domain, RING1, and lobe 1 compose the right segment, whereas lobe 2 forms the left segment of DNMT5.

Methylated CpG dinucleotide recognition

hmDNA binds within a cleft between the HD and CD, with the TRD accessing the DNA through major groove (Figure 2B). In total, 13-bp of the 36-bp DNA encompassing the hemimethylated

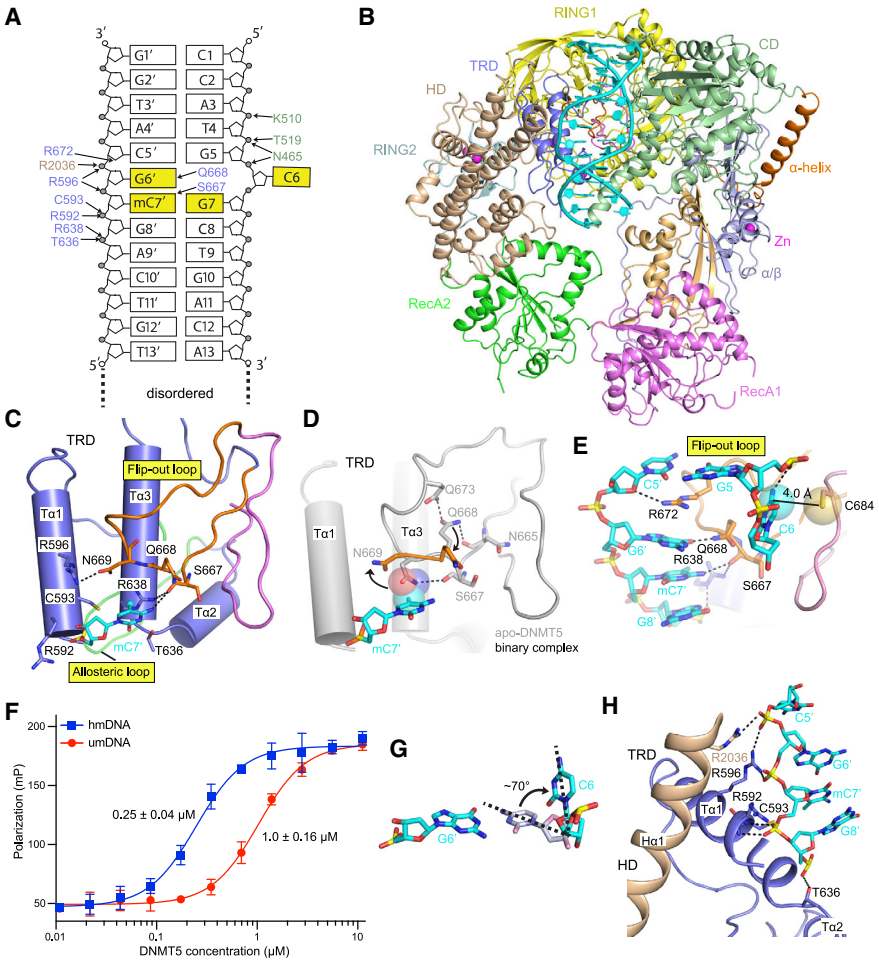

Figure 2. Cryo-EM structure of the DNMT5 binary complex with hmDNA

(A) The sequence of hmDNA including intermolecular contacts with DNMT5.

(B) Ribbon representation of the cryo-EM structure of the DNMT5 binary complex with hmDNA.

(C) 5mC recognition by the TRD.

(D) mC7′ induced conformational change of N669 and Q668 on binary complex formation.

(E) Partial flip out of the target cytosine C6 as a result of the interactions between the TRD and hmDNA.

(F) Fluorescence polarization (FP) assays of FAM-labeled hmDNA and umDNA with an increasing amount of DNMT5. Error bars represent SD; n = 3.

(G) The partial flip out of the target cytosine C6.

(H) Interactions of DNMT5 with the phosphate backbone of the hmDNA-methylated strand.

See also Figures S1, S2, and S3.

CpG site are visible in the binary complex map, implying that the remaining flanking dsDNA is flexible and does not form stable contacts with the ATPase domain.

Sequence-specific intermolecular contacts between DNMT5 and hmDNA (Figure 2A) are made through the TRD. DNMT5 recognizes the 5mC (mC7′) by a hydrogen bond between the main-chain carbonyl of S667 and the N4 of mC7′ base (Figure 2C), which confers preference of 5mC over thymine. The 5-methyl group of mC7′ is accommodated in a shallow basic pocket within the TRD (Figures 2C and S3A). Such a 5mC accommodation is in marked contrast to the corresponding pocket in the structure of the DNMT1-hmDNA complex, where the methyl group of 5mC is anchored within a hydrophobic concave surface (Song et al., 2012). This suggests a different 5mC recognition mechanism in DNMT5.

Structural comparison of apo-DNMT5 and its binary complex reveals that the side chain of N669 occupies the methyl binding pocket in apo-DNMT5 (Figures 2D and S3B). The binding of mC7′ shifts the side chain of N669 away from the pocket to interact with the Tα1 helix of TRD (Figure 2C). The conformational change of N669 in turn releases the side chain of Q668 from interactions with Q673 and N665 (Figure 2D), thereby positioning Q668 for recognition of the orphan guanine G6′ in the methylated CpG dinucleotide (Figure 2E). In the case of binding to umDNA, the side chain of N669 cannot be shifted away to initiate orphan guanine recognition. DNMT5 shows about 4-fold binding preference for hmDNA over umDNA of identical sequence (Figure 2F). The Hill slopes of the fitted curves are about 1.8, suggesting positive cooperativity and additional allosteric conformational changes induced by hmDNA and umDNA binding that further facilitate DNA interaction.

A novel partial flip out of the target cytosine

The side chain of R672 penetrates deep into the DNA duplex forming a hydrogen bond with the deoxyribose sugar oxygen of C5′, with the guanidinium group sandwiched by the G6′ and C5′ bases (Figure 2E). The target cytosine (C6) partially flips out of the DNA duplex, oriented ~70° from its pairing position (Figure 2G), which is then stabilized by a hydrogen bond with the G5 phosphate (Figure 2E). C684 is in the proximity of the 5-carbon of the target cytosine pyrimidine ring (distance of 4.0 Å) (Figure 2E). It appears that C684 is positioned to sense the methylation state of the target cytosine, as a methyl group at 5-carbon would introduce steric hindrance. Interestingly, C684 is not the catalytic cysteine that initiates the methylation reaction.

This partially flipped-out state is strikingly different from the fully flipped-out state observed in other DNMTs or proteins and enzymes involved in writing, reading, and erasing modified bases (Hong and Cheng, 2016; Klimasauskas et al., 1994). The partial base flipping does not require ATP because the target cytosine adopted the same partial flipped-out conformation in the cryo-EM structure of DNMT5 solved by incubation with hmDNA and SAM but without AMP-PNP (designated pseudoternary complex solved at 3.7 Å resolution; Table 1) (Figure S3C). Notably, SAM density was not observed in the pseudoternary complex map.

DNMT5 makes sequence-specific contacts only within the methylated CpG dinucleotide of bound hmDNA (Figure 2A),

Table 1. Statistics of cryo-EM data collection and model refinement

	Apo-DNMT5	Binary complex	Quaternary complex	Pseudoternary complex
Data collection and processing				
Microscope	Titan Krios G2		Titan Krios G2	Titan Krios G2
Detector	Gatan K3		Gatan K3	Gatan K3
Magnification (×)	22,500		22,500	22,500
Voltage (kV)	300		300	300
Electron exposure (e^{-}/Å^2)	53		53	53
Exposure rate (e^{-}/pixel/s)	20		20	20
Number of frames per movie	40		40	40
Defocus range (μm)	−1.0 to −2.5		−1.0 to −2.5	−1.0 to −2.5
Pixel size (Å)	1.064		1.064	1.064
Micrographs (collected/used)	3,185/1,362		6,169/2,608	3,510/2,250
Total extracted particles (no.)	1,323,972		2,439,273	1,833,397
Refined particles (no.)	325,656		87,829	117,289
Final particles (no.)	72,216	78,477	23,621	50,146
Resolution (global)				
FSC 0.5 (unmasked/masked, Å)	3.9/3.6	3.5/3.2	4.1/3.7	3.9/3.8
FSC 0.143 (unmasked/masked, Å)	3.3/3.3	3.1/3.0	3.6/3.5	3.7/3.7
Map sharpening B factor (Å^2)	−66.47	−63.72	−69.86	−95.46
Refinement				
Initial model used	binary complex	*de novo*	binary complex	binary complex
Refinement package	Phenix	Phenix	Phenix	Phenix
Model resolution	3.60	3.19	3.68	3.82
FSC threshold	0.5	0.5	0.5	0.5
Map correlation coefficient	0.80	0.85	0.82	0.82
Model composition				
Nonhydrogen atoms	14,500	14,979	15,239	14,359
Protein residues	1,834	1,830	1,881	1,752
Nucleotide	0	25	18	25
Ligands	5	5	7	5
B factor (Å^2)				
Protein residues	59.58	50.87	43.96	45.05
Nucleotide	–	64.34	88.8	58.32
Ligands	101.64	79.75	36.09	87.17
RMS deviations				
Bond lengths (Å)	0.008	0.008	0.003	0.010
Bond angles (°)	1.000	0.779	0.763	0.994
Validation				
MolProbity score	2.10	2.11	2.11	2.06
Clashscore	11.56	11.71	13.30	11.11
Rotamer outliers (%)	0.06	0.38	0.25	0.00
Cβ outliers (%)	0.0	0.0	0.0	0.0
Ramachandran plot				
Favored (%)	90.98	91.97	93.03	91.74
Allowed (%)	9.02	8.03	6.97	8.26
Disallowed (%)	0.0	0.0	0.0	0.0
PDB code	7R76	7R77	7R78	7T02
EMDB code	EMD-24292	EMD-24294	EMD-24295	EMD-25577

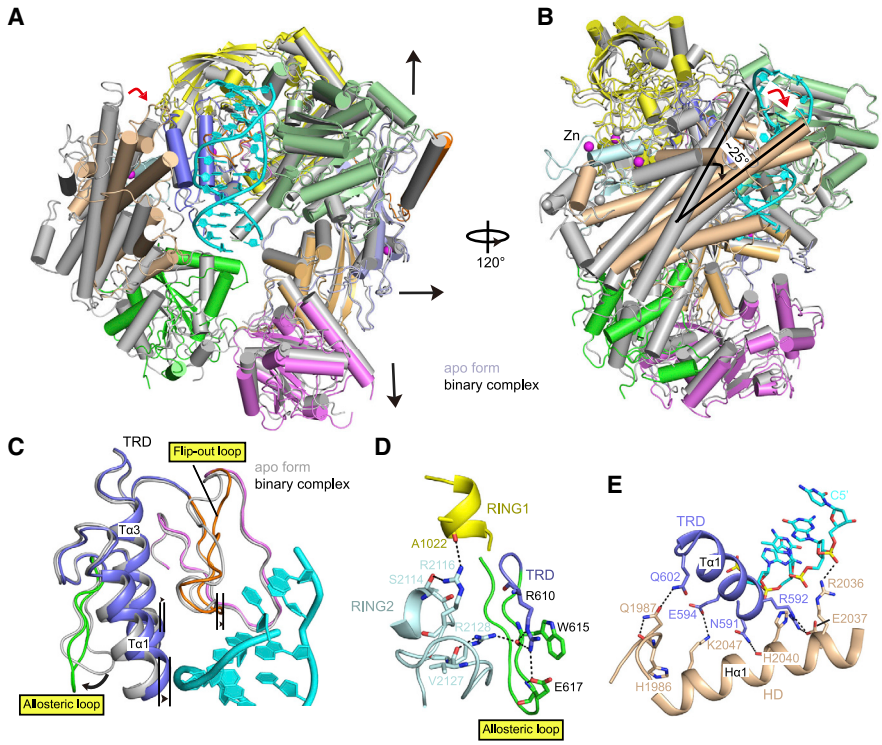

Figure 3. Conformational changes in DNMT5 induced by hmDNA binding

(A and B) hmDNA binding induces conformational changes that expand the right segment (A) and rotate the left segment of DNMT5 (B).

(C) hmDNA recognition by the TRD releases the allosteric loop.

(D) Interactions between the allosteric loop and RING2, as well as between RING1 and RING2.

(E) The hmDNA-induced conformational changes stabilized by interactions between the TRD and HD, as well as between the HD and hmDNA.

See also Figure S3.

consistent with the lack of flanking sequence preference (Catania et al., 2020; Dumesic et al., 2020). hmDNA is further anchored by nonsequence-specific intermolecular interactions with DNMT5 (Figures 2H and S3D). R2036 from the HD makes direct contact with the hmDNA backbone (Figure 2H).

hmDNA induces profound conformational changes in DNMT5

Two views of the superposition of the structures of apo-DNMT5 and the binary complex are shown in Figures 3A and 3B. The binding of hmDNA induces profound conformational changes in DNMT5, primarily observed within the left segment (Video S1). The sequence-specific recognitions by the flip-out loop (Figure 2E) facilitate the Tα1 and Tα3 helices of TRD to move closer to the DNA (Figure 3C). These movements disrupt the hydrogen-bond network locking the allosteric loop in the apo-DNMT5 structure (Figures 1E and S3E). The released allosteric loop contacts RING2, and RING1 also interacts with RING2 (Figure 3D). As a result, the left segment of DNMT5 undergoes a substantial ~25° clockwise rigid body rotation on binary complex formation (Figures 3B and S3F), in which the two zinc atoms in the RING2 move by 24.9 and 16.7 Å, respectively (Figure S3G). The rotated conformation is further stabilized by interactions between the TRD and HD as well as between hmDNA and R2036 from the HD (Figure 3E).

hm DNA binding also impacts on the right segment of DNMT5, with the CD and RING1 moving upward, the α/β region moving toward the right, and the RecA1 moving downward (see arrows in Figure 3A).

hmDNA binding overcomes autoinhibition in the SNF2 ATPase domain

DNMT5 exhibits a basal ATPase activity of approximately 1 min^{-1}, which can be stimulated ~9-fold by hmDNA (Dumesic et al., 2020). The comparable binding affinities of DNMT5 with AMP-PNP without and with hmDNA (Figure S3H) cannot account for the stimulation. Structural analysis shows that the ATPase domain adopts an autoinhibitory conformation in the apo-DNMT5 structure. The Rα3 helix from RecA1 is in a face-to-face position with the Rα13 helix from RecA2 (Figure 4A) that would introduce a steric clash between the two RecA-like domains following formation of an ATP-induced closed conformation. The hmDNA-induced rigid body rotation moves the Rα13 helix away, thereby realigning the two RecA-like domains to allow domain closure for hydrolyzing ATP (Figure 4A). We mutated the Rα13 helix to a GGS-rich loop (GS mutant) to relieve the autoinhibition. Indeed, the autoinhibitory effect was alleviated by ~3.5-fold relative to wild-type (WT) DNMT5 in the absence of DNA (Figure 4B). The E637A mutant, which should facilitate release of the allosteric loop (Figure 1E), also increased

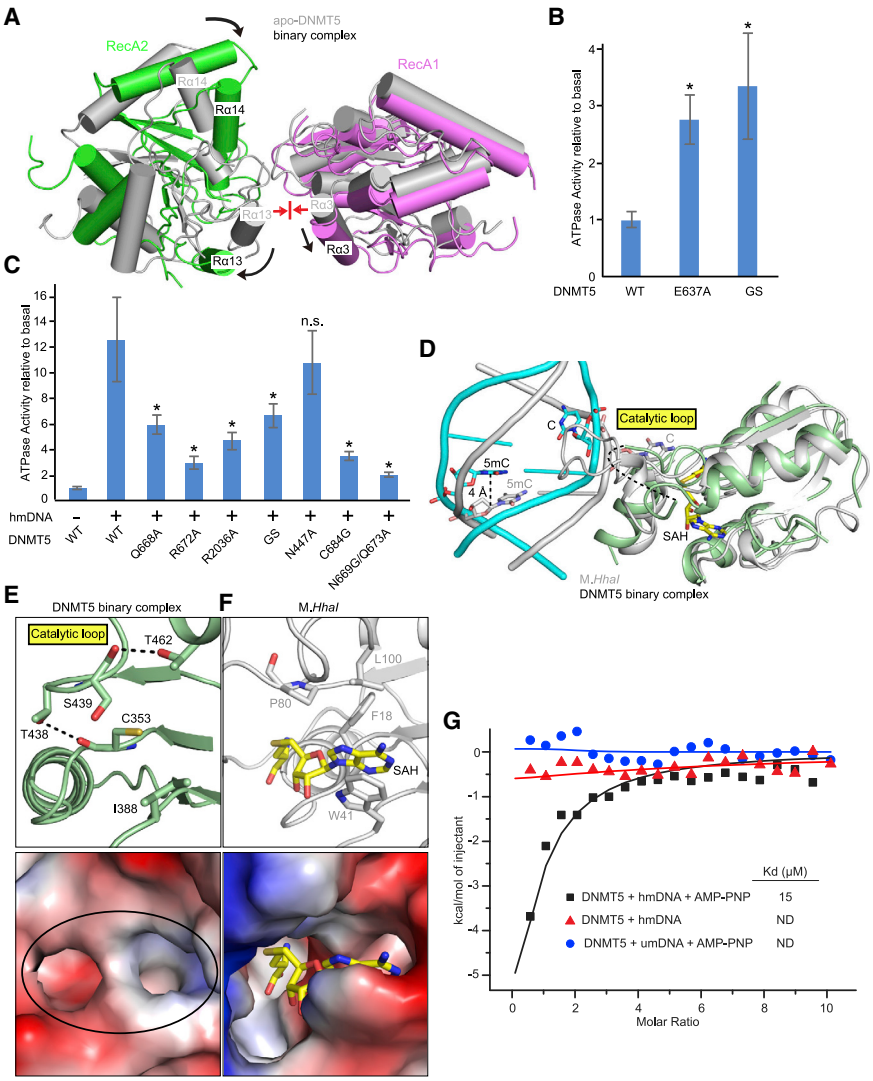

Figure 4. hmDNA stimulates ATPase activity, whereas MTase activity remains suppressed on binary complex formation

(A) The realignment of the two RecA-like domains induced by hmDNA binding.

(B and C) ATPase activity assay of wild-type (WT) and mutants of DNMT5 in the absence of DNA (B) and in the presence of hmDNA (C). Error bars represent SD; n = 4. * Indicates p value < 0.01 in relation to the WT data (B) or WT in the presence of hemimethylated DNA data (C). n.s., not statistically significant.

(D) Structural comparison of the DNMT5 binary complex with the M.HhaI ternary complex with hmDNA and SAH (PDB: 5MHT).

(E and F) Ribbon (top) and electrostatic surface (bottom) representation of the catalytic pockets in the DNMT5 binary complex (E) and in the M.HhaI ternary complex (PDB: 5MHT) (F).

(G) ITC curves of SAH titrated into DNMT5 with indicated DNA or ligands. ND, not detectable.

See also Figures S3 and S4.

the basal ATPase activity ~2.5-fold (Figure 4B). These biochemical data support our "activation by rotation" model for ATPase activation.

We next mutated key residues involved in hmDNA recognition to test their impact on hmDNA-stimulated ATPase activity (Figure 4C). The ATPase activity of the N669G/Q673A double mutant, whose side chain cannot be shifted away to interact with the Tα1 helix (Figure 2C), is least stimulated by hmDNA, even though the lock involving the Q668 side chain is weakened by the Q673A mutation. Disruption of the orphan guanine recognition through Q668A mutation (Figure 2E) reduces the ATPase activity ~2-fold. Mutation of R672, which facilitates the partial flip out of the target cytosine through insertion into the duplex (Figure 2E), results in a 4-fold ATPase activity decrease. The ATPase activity of the R2036A mutant could not be effectively stimulated by hmDNA due to the disruption of the interaction between the HD and hmDNA backbone (Figure 2H). Replacement of the C684 that is positioned to sense the methylation state of the target cytosine by glycine (Figure 2E) reduces the ATPase activity more than 3-fold. These data are consistent with the structural analysis.

The MTase is inactive in the binary complex

A DALI (Holm, 2020) search using the structure of the MTase domain in the DNMT5 binary complex revealed *Hhal* methyltransferase (M.HhaI, PDB: 3EEO) as the top hit (*Z* score 25.2). Structural alignment shows that the structure of DNMT5 MTase domain in the binary complex superposes well with the M.HhaI ternary complex with hmDNA and SAH (O'Gara et al., 1996), with an RMSD of 3.0 Å for 140 Cα atoms (Figure 4D). However, the positions of hmDNA are strikingly different, with the 5mC-G step in the DNMT5 binary complex positioning 4 Å above that in the M.HhaI ternary complex (Figure 4D), such that the catalytic loop of DNMT5 cannot insert into the DNA duplex, with most of the loop invisible due to flexibility.

Notably, a small visible segment of the catalytic loop is stabilized by a hydrogen-bond network involving T438, C353, S439, and T462 in the DNMT5 binary complex (Figure 4E, top). We compared the catalytic pocket of the MTase domain in the DNMT5 binary complex with its counterpart in the M.HhaI ternary complex (Figure 4F). The side chains of the small visible segment of the catalytic loop in the DNMT5 binary complex would introduce steric clashes with the bound SAH (Figure 4E, bottom), thereby preventing cofactor binding. Indeed, no binding was detected when SAH was titrated into hmDNA preincubated DNMT5 without AMP-PNP monitored by isothermal titration calorimetry (ITC) (Figure 4G). This finding is also consistent with the absence of SAM density in the pseudoternary complex map. The majority of the catalytic loop is also invisible in apo-DNMT5, and the small

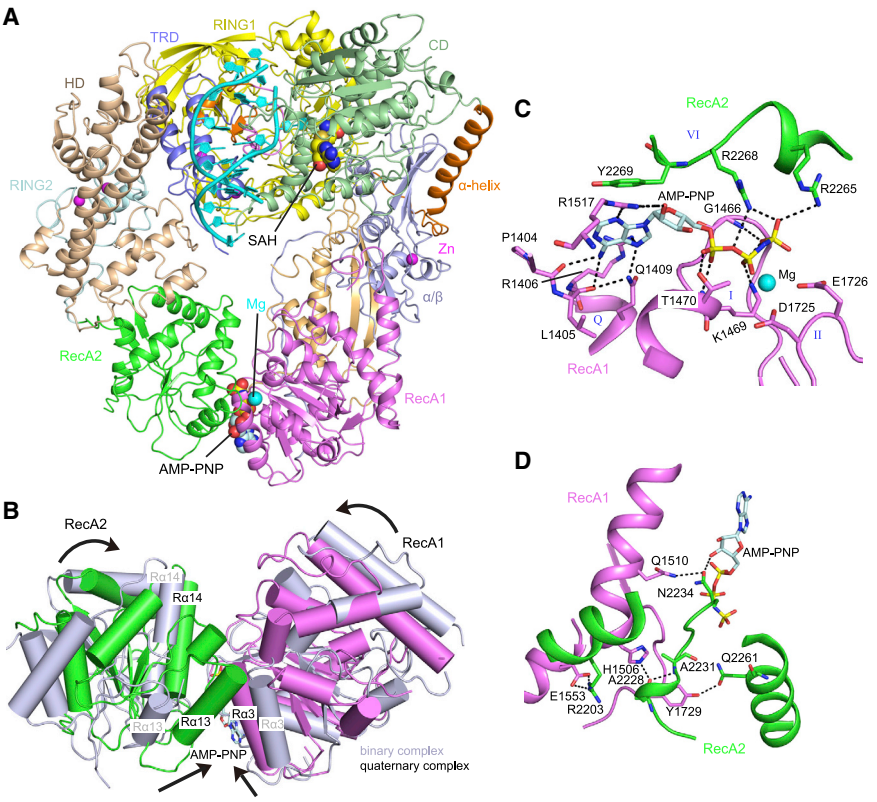

Figure 5. Cryo-EM structure of the DNMT5 quaternary complex

(A) Ribbon representation of the cryo-EM structure of the DNMT5 quaternary complex with hmDNA, AMP-PNP, and SAH.

(B) The closed conformation of the ATPase domain induced by AMP-PNP binding.

(C) AMP-PNP-mediated interactions with RecA1 and RecA2 domains.

(D) Hydrogen bonding interactions between RecA1 and RecA2 domains.

See also Figures S5 and S6.

visible catalytic loop segment acts as a lid to close the catalytic pocket blocking SAM access to both apo-DNMT5 (Figure S3I) and its binary complex (Figure 4E). These findings provide a mechanistic explanation for no MTase activity for the binary complex in the absence of ATP (Figure 1B). Interestingly, the residues forming the hydrogen-bond network (Figure 4E) locate in the conserved motifs I-V (Figure S4) of DNA cytosine-5 methyltransferases that are responsible for SAM binding (Kumar et al., 1994; Lauster et al., 1989; Pósfai et al., 1989). This indicates that DNMT5 may regulate the SAM binding to achieve ultrahigh specificity.

AMP-PNP binding induces a closed conformation in the ATPase domain

The limited binding preference for hmDNA and ATPase activity stimulation cannot explain the remarkable specificity of DNMT5. To further investigate molecular mechanisms underlying the remarkable specificity, we generated DNMT5 quaternary complex by incubation with hmDNA, AMP-PNP, and SAH, followed by direct loading on the cryo-EM grids without further gel filtration purification. The quaternary complex structure was solved at 3.5 Å resolution with the densities for AMP-PNP and SAH readily traceable (Figures 5A and S5; Table 1).

The two RecA-like domains form a closed conformation upon AMP-PNP binding, with the cleft between the two domains closing around the bound ATP analog (Figure 5B). AMP-PNP binds primarily within RecA1, with residues from RecA2 contributing to recognition (Figure 5C). RecA1 contains the classic Q, I, II, and III motifs, whereas RecA2 contains the IV, V, and VI motifs (Fairman-Williams et al., 2010) (Figure S6). K1469 and T1470 of motif I are hydrogen bonded to the α- and β-phosphates of AMP-PNP, whereas D1725 and E1726 of motif II coordinate the Mg^{2+} cation positioned between the β- and γ-phosphates (Figure 5C). R2268 and R2265 of motif VI are coordinated to the γ-phosphate.

The adenosine ring of AMP-PNP is sandwiched through stacking with a tyrosine (Y2269) from motif VI in one direction and with the Q-motif, with which it forms intermolecular contacts, in the opposite direction (Figure 5C). A similar stacking platform sandwiching the adenine ring of cofactor is also observed in SF1 helicases, except that the aromatic residue is located in motif IIIa (Fairman-Williams et al., 2010). Such a two-directional sandwiching interaction appears to facilitate the ATPase domain to adopt a closed conformation more effectively in the ATP bound form. By contrast, a conserved tyrosine is positioned within the Q-motif of ISW1 and SWR1 (Figure S6), which are nucleosome remodelers of the SNF2 family and whose structures have been reported in complex with nucleosome core particles (Willhoft et al., 2018; Yan et al., 2019), therefore enabling stacking from one direction. In addition to the AMP-PNP-mediated interactions between the two RecA-like domains, residues from both domains also form direct hydrogen-bond interactions (Figure 5D).

We also compared the ATPase domains of DNMT5, ISW1. and SWR1. The key residues, locating within Ia-c, IV, IVa, V, and Va motifs, that are required for DNA binding in chromatin remodelers (Fairman-Williams et al., 2010) are not conserved in DNMT5 (Figure S6). In addition, no density of interacting DNA is observed near the ATPase domain in the maps of both DNMT5 binary and quaternary complexes. Further, the isolated ATPase domain did not display DNA binding *in vitro* in our earlier study (Dumesic et al., 2020). These data suggest that the ATPase domain of DNMT5 does not harbor DNA binding capacity.

SNF2 ATPase domain closure allosterically activates the MTase domain

The closed conformation of ATPase domain formed upon AMP-PNP binding changes the relative orientation of RecA1 and

CellPress
OPEN ACCESS

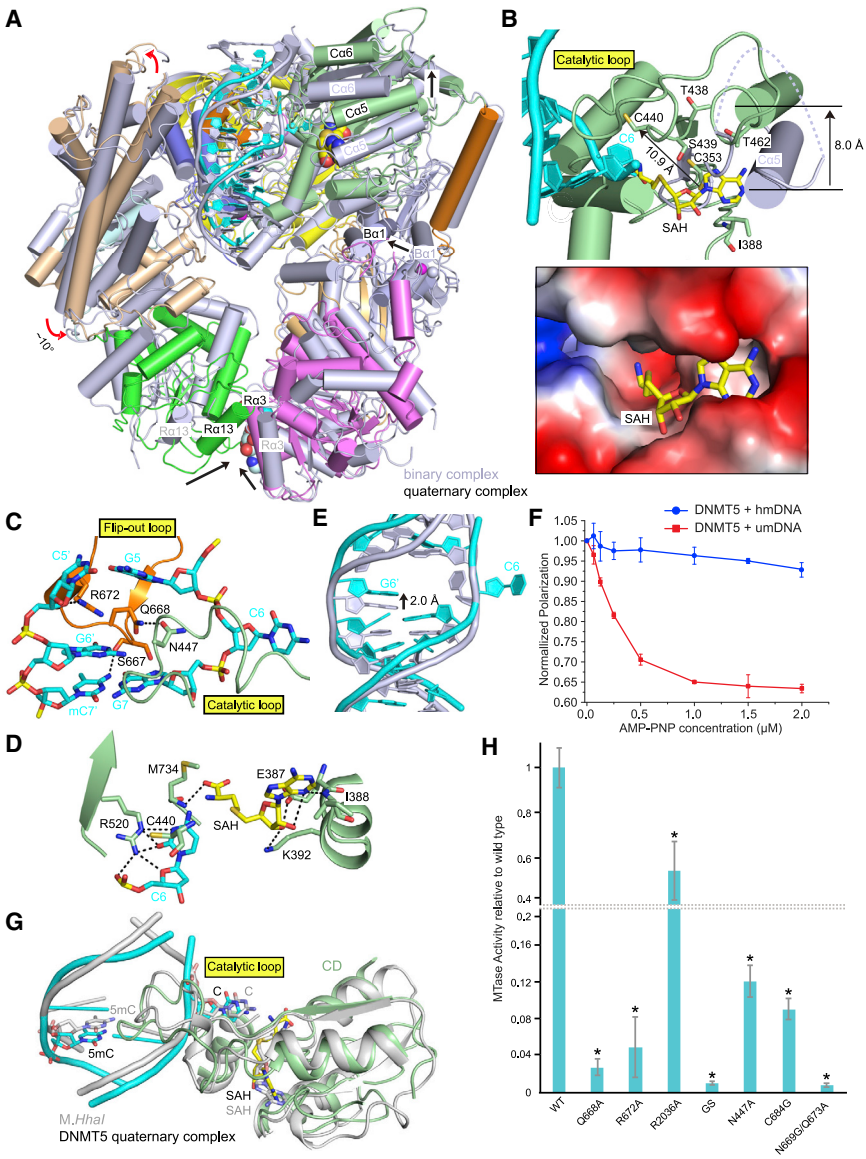

Figure 6. AMP-PNP binding to the ATPase domain activates the DNMT5 MTase domain

(A) Conformational changes induced by AMP-PNP binding on proceeding from the DNMT5 binary complex to the quaternary complex.

(B) Conformational changes in the catalytic pocket on proceeding from the DNMT5 binary complex (without bound SAH, in silver) to the quaternary complex (contains bound SAH, in color) (top) and electrostatic surface representation of the catalytic pocket in the quaternary complex (bottom).

(C) Insertion of the catalytic loop into hmDNA and the complete base flipping of target cytosine.

(D) Positioning of SAH within the MTase domain and its alignment relative to the target cytosine C6 and catalytic cysteine C440.

(E) Overlay of the hmDNA from binary (in silver) and quaternary (in color) complexes.

(F) FP assays of hmDNA and umDNA (FAM-labeled) preincubated DNMT5 with an increasing amount of AMP-PNP. Error bars represent SD; n = 3.

(G) Structural comparison of the DNMT5 quaternary complex with the M.HhaI ternary complex (PDB: 5MHT).

(H) MTase activity of DNMT5 WT and mutants on the hmDNA substrate. Error bars represent SD; n = 4. * indicates p value < 0.01 in relation to the WT data.

See also Figure S7.

RecA2 (Figure 5B). These changes are propagated to both segments of DNMT5, resulting in substantial conformational changes and an overall more compact structure (Figure 6A; Video S2)

The conformational changes associated with RecA1 propagate through the RecA1 insertions to the α/β region and upward to the MTase domain. The MTase domain is lifted by the inward movements of α/β region such that the Cα5 helix following the catalytic loop is raised by ~8 Å, allowing the catalytic loop to insert in the DNA duplex (Figure 6B). Notably, the catalytic loop is visible along its entire length in the quaternary complex, in contrast to most of it being invisible due to flexibility in the binary complex. The side chain of N447 from the catalytic loop inserts into hmDNA from the minor groove direction, whereas the flip-out loop of the TRD approaches the DNA from the major groove direction (Figure 6C). Q668 from the flip-out loop, which recognized G6′ in the binary complex, now shifts to stabilize the catalytic loop by forming a hydrogen bond with N447 (Figure 6C). The target cytosine C6 flips completely out of the DNA duplex into the catalytic pocket of the MTase domain and is further stabilized by the side chain of R520 (Figure 6D). Importantly, the catalytic cysteine C440 within the catalytic loop also moves 10.9 Å from its position in the binary complex and locates near the target cytosine C6 (Figure 6B; Video S2).

The insertion of the catalytic loop into hmDNA disrupts the hydrogen bonds stabilizing its small segment in the binary complex (Figure 4E) and opens the catalytic pocket for SAH binding (Figure 6B). SAH is bound in the proximity of the flipped-out cytosine and catalytic cysteine, with the adenosine base hydrogen bonded to the main chain of I388, the sugar ring hydrogen bonded to the side chains of E387 and K392, and the carboxy tail stabilized by hydrogen bonding with M734 (Figure 6D). The binding affinity of SAH to DNMT5 is ~15 μM in the presence of hmDNA and AMP-PNP (Figure 4G). The MTase domain, hmDNA, and SAH in the DNMT5 quaternary complex superpose well (RMSD of 1.6 Å for 131 Cα atoms) with that of the M.HhaI ternary complex (Figure 6G), suggestive of a potentially productive conformation.

Single turnover MTase experiments (enzyme excess) shows that AMP-PNP is able to induce MTase activity (Figure S7A). This activity is not due to contaminating ATP or slow hydrolysis

of AMP-PNP, as hydrolysis product (ADP or free phosphate) cannot be detected even in the presence of hexokinase (Figures S7B and S7C). However, kinetic analysis showed a ~1000-fold lower catalytic rate in the presence of AMP-PNP compared with ATP (Figure S7D). These findings indicate that nucleotide binding indeed places the enzyme in a conformation very close to the fully catalytic conformation, but hydrolysis is required for biologically meaningful activity.

Nucleotide binding ensures substrate specificity

Upon proceeding from the binary complex to the quaternary complex, the movement of RecA2 in the left segment of DNMT5 results in a ~10° counterclockwise rotation of the rigid HD domain (Figure 6A); this rotation generates space for movement of the MTase domain and hmDNA in an upward direction such that the hmDNA is lifted by about 2 Å (Figure 6E). This lift and the overall compact conformation in the quaternary complex would be a challenge for the nonspecifically bound umDNA because of fewer contacts with DNMT5. We measured the fluorescence polarization (FP) of umDNA and hmDNA (FAM-labeled) preincubated DNMT5 with increasing amounts of AMP-PNP. Strikingly, the polarization of the DNMT5-umDNA complex decreases on addition of AMP-PNP, whereas that of the DNMT5-hmDNA complex is minimally affected (Figure 6F), demonstrating that nonspecifically bound umDNA is dissociated from DNMT5 upon AMP-PNP binding. The unlabeled umDNA and hmDNA competition FP assays with and without AMP-PNP also show that about 60% FAM-labeled umDNA is ejected by AMP-PNP binding resulting in a flat umDNA competition curve (Figure S7E). By contrast, the labeled hmDNA is little affected by AMP-PNP binding and shows a similar hmDNA competition curve with that in absence of AMP-PNP. AMP-PNP can only mimic the pre-hydrolytic state of ATP hydrolysis (Lacabanne et al., 2020). Our kinetic analysis (Figure S7D) also indicates that ATP hydrolysis is required to enable fully activated MTase activity. ATP hydrolysis may induce additional conformational changes to completely eject the bound unmethylated DNA.

ITC experiments showed no detectable binding of SAH to umDNA preincubated DNMT5 in the presence of AMP-PNP (Figure 4G). Thus, the catalytic pocket of MTase domain remains closed with noncognate umDNA substrate, and AMP-PNP binding results in the release of the umDNA, which contrasts with opening the catalytic pocket for hmDNA substrate. These findings explain the lack of MTase activity on umDNA in the presence of ATP (Figure 1B). We conclude that access of SAM to the catalytic pocket of DNMT5 MTase domain is controlled by its ATPase domain which licenses hmDNA for catalysis, ejects noncognate umDNA and enables the system to achieve its remarkable specificity.

Finally, to test the relevance of the structural observations, we measured the MTase activity of DNMT5 mutants in the presence of hmDNA (Figure 6H). Alanine mutations of residues involved in 5mC recognition or partial flip out of the target cytosine, such as N669/Q673, Q668, and R672, exhibit predominant loss of MTase activity on hmDNA, emphasizing the importance of hmDNA recognition. Disruption of the interaction between the HD and hmDNA backbone by the R2036A mutation reduces the catalytic activity by half relative to WT. The replaced GGS loop also shows low methylation activity. The relative MTase activity of the N447A mutant, which displays no defect in ATPase activity (Figure 4C), is reduced by almost 10-fold, supporting the role for N447 insertion into the DNA duplex. The C684G mutant also exhibits a reduction in methylation activity. These data support the predictions of the structural data.

DISCUSSION

DNMT5 is the only known ATP-dependent DNA cytosine-5 methyltransferase that displays exquisite specificity for hemimethylated DNA and, unexpectedly, mediates epigenome evolution over million-year timescales (Dumesic et al., 2020; Catania et al, 2020). Our structural and biochemical analyses reveal a stepwise allosteric cascade triggered by hmDNA binding that culminates in the completion of the construction of a MTase active site. Our studies also reveal how communication between the ATPase and MTase domains occurs and how the remarkable specificity of DNMT5 is achieved. We discuss below how these communications occur at the molecular level to drive a hmDNA- and ATP-dependent allosteric cycle and how substrate recognition impinges on this cycle at multiple steps. Together, they provide the first structural basis for understanding faithful, ATP-dependent epigenetic memory.

hmDNA recognition triggers a stepwise allosteric cascade

The ATPase domain of DNMT5 exhibits low basal activity in the absence of hmDNA substrate in which its activity is regulated by an autoinhibitory mechanism. A pair of α-helices in the ATPase domain are positioned to prevent RecA1 and RecA2 from forming a closed conformation (Figure 7A). hmDNA is recognized by DNMT5 through a "trigger mechanism," like the first domino in a series falling, to reposition the side chain of N669 due to contacts by the methyl group of 5mC, which initiates the specific recognition of the orphan guanine by Q668 and subsequent conformational changes. The target cytosine is flipped partially out of the DNA duplex such that its unmethylated state is sensed by C684. The signal of hmDNA binding read by the MTase domain is communicated to the ATPase domain through release of the allosteric loop to contact with the RecA2 insertion, resulting in a profound rigid body rotation of the left segment of DNMT5 upon binary complex formation. The rotation stimulates the ATPase activity by realigning the two RecA-like domains capable to form a closed conformation for ATP hydrolysis (Figure 7B).

Then, ATP binding to the ATPase domain induces formation of a closed conformation, which is communicated to MTase domain mainly through the RecA1 insertions and the α/β region positioned within the right segment of DNMT5. The catalytic pocket of MTase domain is allosterically remodeled to promote catalytic loop insertion into the DNA duplex. The insertion opens the catalytic pocket for SAM entry, facilitates complete base flipping of the target cytosine into the active site, and brings the catalytic cysteine into proximity to initiate methyl group transfer from SAM (Figure 7C). ATP binding also ejects noncognate umDNA to ensure substrate specificity. Subsequent SAM binding allows DNA methylation reaction to proceed (Figure 7D), and ATP hydrolysis enables a fully catalytic conformation (Figure 7E).

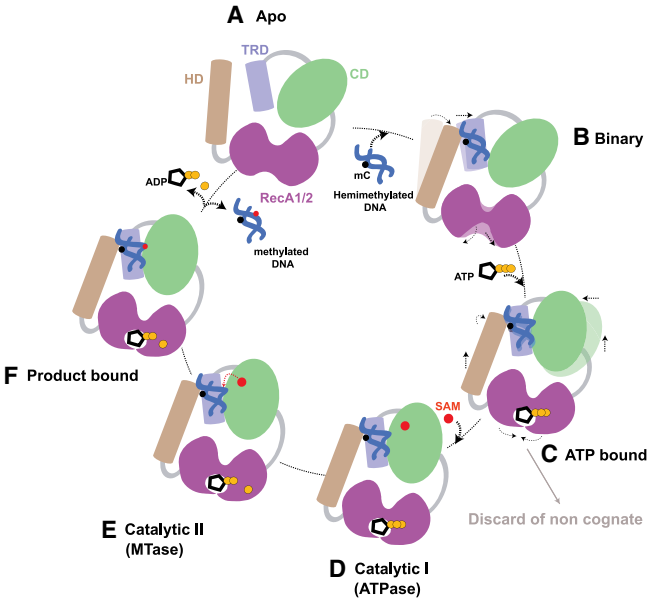

Figure 7. Model of the DNMT5-mediated methylation cycle

(A) The ATPase domain adopts an autoinhibitory conformation that restricts DNMT5 with low basal activity in the apo state.

(B) Specific recognition of hmDNA by the MTase domain stimulates the ATPase activity through a rigid body rotation to overcome the autoinhibitory conformation.

(C) ATP binding to the ATPase domain remodels the MTase domain, opens the catalytic pocket for SAM binding on the hmDNA substrate, and licenses post-DNA-binding ejection on the umDNA substrate.

(D) Entry of SAM into the catalytic pocket.

(E) ATP is hydrolyzed, fully activating the MTase to enable methyl-transfer from SAM.

(F) Product-bound state after catalysis.

A stable partially flipped-out state of the target cytosine

We observed a novel stable partially flipped-out state of the target cytosine in the binary complex (Figure 2E), which has not been seen in other proteins and enzymes involved in writing, reading, and erasing modified bases (Hong and Cheng, 2016; Klimasauskas et al., 1994). A ^{19}F NMR spectral study supported an ensemble of flipped-out forms equilibrating between a stacked form in the B-DNA and the completely flipped-out form (observed in the crystal structure of the M.HhaI ternary complex) (Klimasauskas et al., 1998). However, the flipped-out cytosine base is dynamic and lacks a clear preferred conformation in the above study, which is different from the stable partially flipped-out state observed in DNMT5. Methylated CpG dinucleotide recognition induces the target cytosine to partially flip out of the DNA duplex. It appears that the partial flip out of target cytosine does not need invasion of the catalytic loop into the DNA duplex, given that the catalytic loop is invisible due to flexibility in the structure of the binary complex. DNA breathing (Chen and Prohofsky, 1995) may also play a role during partial base flipping.

The partially flipped-out state of target cytosine is critical for the eventual success of DNA methylation as mutations of residues involving in forming this intermediate state severely impair MTase activity (Figure 6H). The intermediate state may lower the free-energy barrier to achieve the completely flipped-out state. It is worth noting that the complete cytosine base flipping in DNMT5, not the partially flipped-out state, needs ATP binding to the ATPase domain. The partially flipped-out cytosine might constitute a second proofreading step following the initial 5mC recognition to discriminate hmDNA and fully methylated DNA (fmDNA).

The MTase domain requires remodeling to be active

Unlike other DNMTs, the activity of the MTase domain of DNMT5 is allosterically regulated by the control of methyl donor SAM binding. Structure-based sequence alignment shows that the MTase domain of DNMT5 contains all conserved motifs of DNA cytosine-5 methyltransferases (Kumar et al., 1994; Lauster et al., 1989; Pósfai et al., 1989), except some residue substitutions in motifs I-V that are responsible for SAM binding (Figure S4). The conserved aromatic residues in motifs I and II of M.HhaI (F18 and W41) are replaced with small side-chain residues (C453 and I388) in DNMT5 (Figures 4E and 4F). Additionally, hydrophobic residues (P80 and L100) in motifs IV and V of M.HhaI are changed to hydrophilic residues in DNMT5 (S439 and T462). By contrast to the tight binding of SAM to M.HhaI during purification (Kumar et al., 1992), these residue substitutions should weaken the binding of SAM to DNMT5 and make the SAM binding regulatable. Importantly, the proline in the absolutely conserved catalytic cysteine-containing prolylcysteinyl (PC) dipeptide located in motif IV of M.HhaI (Kumar et al., 1992; Lauster et al., 1989; Pósfai et al., 1989) is replaced by S439 in DNMT5. The *S. pombe* DNMT2 also has the serine substitution, which was thought to be functionally nonactive as a result of the substitution (Pinarbasi et al., 1996). Afterward, DNMT2 was shown to be a tRNA methyltransferase (Goll et al., 2006; Johansson et al., 2018). Interestingly, these residue substitutions within DNMT5 generates a hydrogen-bond network stabilizing part of the catalytic loop that closes the catalytic pocket as a lid and prevents SAM from binding in apo-DNMT5 and binary complex. Sequence alignment of DNMT5 among other fungi and protists shows that the residue substitutions observed in DNMT5 are very conserved (Figure S7F). This suggests that the regulation mechanism of the DNMT5 MTase domain is conserved in fungi and protists. Additionally, hmDNA binds to DNMT5 in a position that is higher than that observed in the M.HhaI complex (Figure 4D), resulting in the DNMT5 catalytic loop unable to insert into the DNA duplex. These features enable the MTase domain of DNMT5 to be subjected to regulation.

A novel enzyme-remodeling role of the SNF2 ATPase domain

SNF2 ATPases are best known for their role as chromatin remodeling enzymes (Flaus et al., 2006). Here, we describe an SNF2 ATPase that remodels the catalytic pocket of the adjoined regulatable MTase domain to enable remarkable substrate specificity. Nucleotide binding to the SNF2 ATPase domain allosterically opens the catalytic pocket in the MTase to allow SAM cofactor binding and triggers DNA modification specifically on the hmDNA substrate produced by DNA replication. Importantly, umDNA binding leads to a different outcome, in which the pocket remains closed upon ATP binding, with umDNA instead ejected from the enzyme-substrate complex.

In this sense, the SNF2 ATPase domain of DNMT5 acts in a chaperone-like manner to complete folding and positioning of a catalytic domain into an active conformation. This active site remodeling allows SAM access to the catalytic pocket and the completion of base flipping into the active site. These findings help to explain the extraordinary specificity of DNMT5, which presumably enables it to mediate epigenetic evolution over geological timescales (Catania et al., 2020). As DNMT5 enzymes are found throughout the fungal and protist kingdoms, including important photosynthetic picoeukaryotes (Huff and Zilberman, 2014; Ponger and Li, 2005), it is likely that the principles defined here apply to many organisms, which we predict will be found to harbor the ability to remember their past via DNA methylation, perhaps for long periods of time. Supporting this prediction, alignment of the relevant domains in orthologs in fungi and protists indicate conservation of the key functional residues described here (Figure S7F).

Multiple layered mechanisms contribute to fidelity of epigenetic inheritance

Although the overall recruitment of DNMT5 to chromosomal regions harboring H3K9me via its chromodomain, its association with chromatin recruitment does not explain the remarkable specificity of DNMT5 for hemimethylated DNA. Our studies suggest that multiple, layered mechanisms contribute to this specificity, each of which represents a previously undescribed molecular event.

First, hemimethylated DNA triggers "activation by rotation" of the SNF2 ATPase domain. As discussed above, this post-binding event is mediated by the parental strand cytosine 5-methyl group "nudging" N669, triggering a series of changes in the TRD hydrogen-bond network that result in the activation of the SNF2 ATPase domain for ATP hydrolysis. Second, the catalytic pocket of the MTase domain is regulated by the ATPase domain, such that it only opens upon the binding of DNMT5 to hemimethylated DNA and ATP but remains closed when DNMT5 is bound to unmethylated DNA. Third, ATP binding triggers ejection of unmethylated (noncognate) DNA, suggesting that nucleotide binding enables an additional discrimination step, reminiscent of kinetic proofreading in the ribosome. It is possible that noncognate substrate discard also can occur after ATP hydrolysis but prior to catalysis, which would enable even further discrimination. The overall picture emerges that, combined with chromatin targeting by H3K9me, multiple layers of substrate discrimination conspire to endow the DNMT5 system with the ability to transmit epigenetic information in the form of a heritable DNA modification over long timescales (Catania et al., 2020).

Limitations of the study

The ATPase domain of DNMT5 belongs to a subgroup within the SNF2 family that includes Rad5, Rad16, Ris1, HLTF, and SHPRH, which are characterized by a RING finger insertion within the RecA2-like domain (Flaus et al., 2006). Some RING fingers of this subgroup proteins exhibit E3 ubiquitin ligase activity (Unk et al., 2010). Further study is needed to elucidate whether the RING2 of DNMT5 harbors E3 ubiquitin ligase activity.

Transient states are not easily captured by cryo-EM. Thus, refinement of the model shown in Figure 7 particularly the precise conformation of the post-hydrolysis enzyme and the roles of phosphate and ADP release will require additional structural studies aimed at capturing intermediates coupled with further detailed enzymological investigations.

STAR★METHODS

Detailed methods are provided in the online version of this paper and include the following:

- KEY RESOURCES TABLE
- RESOURCE AVAILABILITY
  - Lead contact
  - Materials availability
  - Data and code availability
- EXPERIMENTAL MODEL AND SUBJECT DETAILS
  - Bacterial cells
  - Insect cells
- METHOD DETAILS
  - Protein expression and purification
  - Cryo-EM sample preparation
  - Cryo-EM data acquisition
  - Image processing
  - Atomic model building and refinement
  - Fluorescence polarization (FP) assay
  - Isothermal titration calorimetry (ITC)
  - ATPase assay
  - DNA methyltransferase assay
- QUANTIFICATION AND STATISTICAL ANALYSIS

SUPPLEMENTAL INFORMATION

Supplemental information can be found online at https://doi.org/10.1016/j.molcel.2022.01.028.

ACKNOWLEDGMENTS

We thank Geeta J. Narlikar and members of her laboratory, especially Emily Wong, for advice on the enzymological experiments. We thank Wei Xie, You Yu, Phillip A. Dumesic, and Garrett M. Warren for helpful discussions and thank Stephen Long for use of the SpectraMax M5 microplate reader. D.J.P. is supported by funding from the Leukemia and Lymphoma Society, the Maloris Foundation, and the Memorial Sloan-Kettering Cancer Center Core grant P30 CA008748. This work was also supported by NIH R01 GM071801 to H.D.M. H.D.M. is an Investigator of the Chan Zuckerberg Biohub.

AUTHOR CONTRIBUTIONS

J.W. undertook all the cryo-EM experiments with the help of C.W. and M.J.d.l.C., as well as the FP and ITC assays, under the supervision of D.J.P. S.C. and H.D.M. designed and provided the insect cell constructs. S.C. and B.R. performed the ATPase and MTase activity assays under the guidance of H.D.M. The paper was written by J.W., D.J.P., and H.D.M. with input from S.C.

DECLARATION OF INTERESTS

The authors declare no competing interests.

Received: September 30, 2021
Revised: January 24, 2022
Accepted: January 26, 2022
Published: February 23, 2022

REFERENCES

Adams, P.D., Afonine, P.V., Bunkóczi, G., Chen, V.B., Davis, I.W., Echols, N., Headd, J.J., Hung, L.W., Kapral, G.J., Grosse-Kunstleve, R.W., et al. (2010). Phenix: a comprehensive Python-based system for macromolecular structure solution. Acta Crystallogr. D Biol. Crystallogr. *66*, 213–221. https://doi.org/10.1107/S0907444909052925.

Arand, J., Spieler, D., Karius, T., Branco, M.R., Meilinger, D., Meissner, A., Jenuwein, T., Xu, G., Leonhardt, H., Wolf, V., et al. (2012). In vivo control of CpG and non-CpG DNA methylation by DNA methyltransferases. PLoS Genet. *8*, e1002750. https://doi.org/10.1371/journal.pgen.1002750.

Bai, X.C., Rajendra, E., Yang, G., Shi, Y., and Scheres, S.H. (2015). Sampling the conformational space of the catalytic subunit of human gamma-secretase. eLife *4*, e11182. https://doi.org/10.7554/eLife.11182.

Biniszkiewicz, D., Gribnau, J., Ramsahoye, B., Gaudet, F., Eggan, K., Humpherys, D., Mastrangelo, M.A., Jun, Z., Walter, J., and Jaenisch, R. (2002). Dnmt1 overexpression causes genomic hypermethylation, loss of imprinting, and embryonic lethality. Mol. Cell. Biol. *22*, 2124–2135. https://doi.org/10.1128/MCB.22.7.2124-2135.2002.

Catania, S., Dumesic, P.A., Pimentel, H., Nasif, A., Stoddard, C.I., Burke, J.E., Diedrich, J.K., Cooke, S., Shea, T., Gienger, E., et al. (2020). Evolutionary persistence of DNA methylation for millions of years after ancient loss of a de novo methyltransferase. Cell *180*, 816. https://doi.org/10.1016/j.cell.2020.02.006.

Chen, Y.Z., and Prohofsky, E.W. (1995). Sequence and temperature dependence of the interbase hydrogen-bond breathing modes in B-DNA polymers: comparison with low-frequency Raman peaks and their role in helix melting. Biopolymers *35*, 573–582. https://doi.org/10.1002/bip.360350603.

Dumesic, P.A., Stoddard, C.I., Catania, S., Narlikar, G.J., and Madhani, H.D. (2020). ATP hydrolysis by the SNF2 domain of Dnmt5 is coupled to both specific recognition and modification of hemimethylated DNA. Mol. Cell *79*, 127–139.e4. https://doi.org/10.1016/j.molcel.2020.04.029.

Emsley, P., Lohkamp, B., Scott, W.G., and Cowtan, K. (2010). Features and development of coot. Acta Crystallogr. D Biol. Crystallogr. *66*, 486–501. https://doi.org/10.1107/S0907444910007493.

Fairman-Williams, M.E., Guenther, U.P., and Jankowsky, E. (2010). SF1 and SF2 helicases: family matters. Curr. Opin. Struct. Biol. *20*, 313–324. https://doi.org/10.1016/j.sbi.2010.03.011.

Flaus, A., Martin, D.M., Barton, G.J., and Owen-Hughes, T. (2006). Identification of multiple distinct Snf2 subfamilies with conserved structural motifs. Nucleic Acids Res. *34*, 2887–2905. https://doi.org/10.1093/nar/gkl295.

Goddard, T.D., Huang, C.C., Meng, E.C., Pettersen, E.F., Couch, G.S., Morris, J.H., and Ferrin, T.E. (2018). UCSF ChimeraX: meeting modern challenges in visualization and analysis. Protein Sci. *27*, 14–25. https://doi.org/10.1002/pro.3235.

Goll, M.G., Kirpekar, F., Maggert, K.A., Yoder, J.A., Hsieh, C.L., Zhang, X., Golic, K.G., Jacobsen, S.E., and Bestor, T.H. (2006). Methylation of tRNAAsp by the DNA methyltransferase homolog Dnmt2. Science *311*, 395–398. https://doi.org/10.1126/science.1120976.

Hashimoto, H., Horton, J.R., Zhang, X., Bostick, M., Jacobsen, S.E., and Cheng, X. (2008). The SRA domain of UHRF1 flips 5-methylcytosine out of the DNA helix. Nature *455*, 826–829. https://doi.org/10.1038/nature07280.

Holm, L. (2020). DALI and the persistence of protein shape. Protein Sci. *29*, 128–140. https://doi.org/10.1002/pro.3749.

Hong, S., and Cheng, X. (2016). DNA base flipping: A general mechanism for writing, reading, and erasing DNA modifications. Adv. Exp. Med. Biol. *945*, 321–341. https://doi.org/10.1007/978-3-319-43624-1_14.

Huff, J.T., and Zilberman, D. (2014). Dnmt1-independent CG methylation contributes to nucleosome positioning in diverse eukaryotes. Cell *156*, 1286–1297. https://doi.org/10.1016/j.cell.2014.01.029.

Johannsson, S., Neumann, P., Wulf, A., Welp, L.M., Gerber, H.D., Krull, M., Diederichsen, U., Urlaub, H., and Ficner, R. (2018). Structural insights into the stimulation of S. pombe Dnmt2 catalytic efficiency by the tRNA nucleoside queuosine. Sci. Rep. *8*, 8880. https://doi.org/10.1038/s41598-018-27118-5.

Klimasauskas, S., Kumar, S., Roberts, R.J., and Cheng, X. (1994). HhaI methyltransferase flips its target base out of the DNA helix. Cell *76*, 357–369. https://doi.org/10.1016/0092-8674(94)90342-5.

Klimasauskas, S., Szyperski, T., Serva, S., and Wüthrich, K. (1998). Dynamic modes of the flipped-out cytosine during HhaI methyltransferase-DNA interactions in solution. EMBO J. *17*, 317–324. https://doi.org/10.1093/emboj/17.1.317.

Kumar, S., Cheng, X., Klimasauskas, S., Mi, S., Posfai, J., Roberts, R.J., and Wilson, G.G. (1994). The DNA (cytosine-5) methyltransferases. Nucleic Acids Res. *22*, 1–10. https://doi.org/10.1093/nar/22.1.1.

Kumar, S., Cheng, X., Pflugrath, J.W., and Roberts, R.J. (1992). Purification, crystallization, and preliminary X-ray diffraction analysis of an M.HhaI-AdoMet complex. Biochemistry *31*, 8648–8653. https://doi.org/10.1021/bi00151a035.

Lacabanne, D., Wiegand, T., Wili, N., Kozlova, M.I., Cadalbert, R., Klose, D., Mulkidjanian, A.Y., Meier, B.H., and Böckmann, A. (2020). ATP analogues for structural investigations: case studies of a DnaB helicase and an ABC transporter. Molecules *25*. https://doi.org/10.3390/molecules25225268.

Lauster, R., Trautner, T.A., and Noyer-Weidner, M. (1989). Cytosine-specific type II DNA methyltransferases. A conserved enzyme core with variable target-recognizing domains. J. Mol. Biol. *206*, 305–312. https://doi.org/10.1016/0022-2836(89)90480-4.

Li, Y., Zhang, Z., Chen, J., Liu, W., Lai, W., Liu, B., Li, X., Liu, L., Xu, S., Dong, Q., et al. (2018). Stella safeguards the oocyte methylome by preventing de novo methylation mediated by DNMT1. Nature *564*, 136–140. https://doi.org/10.1038/s41586-018-0751-5.

Liu, O.W., Chun, C.D., Chow, E.D., Chen, C., Madhani, H.D., and Noble, S.M. (2008). Systematic genetic analysis of virulence in the human fungal pathogen Cryptococcus neoformans. Cell *135*, 174–188. https://doi.org/10.1016/j.cell.2008.07.046.

O'Gara, M., Roberts, R.J., and Cheng, X. (1996). A structural basis for the preferential binding of hemimethylated DNA by HhaI DNA methyltransferase. J. Mol. Biol. *263*, 597–606. https://doi.org/10.1006/jmbi.1996.0601.

Pettersen, E.F., Goddard, T.D., Huang, C.C., Couch, G.S., Greenblatt, D.M., Meng, E.C., and Ferrin, T.E. (2004). UCSF Chimera–a visualization system for exploratory research and analysis. J. Comput. Chem. *25*, 1605–1612. https://doi.org/10.1002/jcc.20084.

Pinarbasi, E., Elliott, J., and Hornby, D.P. (1996). Activation of a yeast pseudo DNA methyltransferase by deletion of a single amino acid. J. Mol. Biol. *257*, 804–813. https://doi.org/10.1006/jmbi.1996.0203.

Ponger, L., and Li, W.H. (2005). Evolutionary diversification of DNA methyltransferases in eukaryotic genomes. Mol. Biol. Evol. *22*, 1119–1128. https://doi.org/10.1093/molbev/msi098.

Pósfai, J., Bhagwat, A.S., Pósfai, G., and Roberts, R.J. (1989). Predictive motifs derived from cytosine methyltransferases. Nucleic Acids Res. *17*, 2421–2435. https://doi.org/10.1093/nar/17.7.2421.

Pradhan, S., Bacolla, A., Wells, R.D., and Roberts, R.J. (1999). Recombinant human DNA (cytosine-5) methyltransferase. I. Expression, purification, and comparison of de novo and maintenance methylation. J. Biol. Chem. *274*, 33002–33010. https://doi.org/10.1074/jbc.274.46.33002.

Pradhan, S., Talbot, D., Sha, M., Benner, J., Hornstra, L., Li, E., Jaenisch, R., and Roberts, R.J. (1997). Baculovirus-mediated expression and characterization of the full-length murine DNA methyltransferase. Nucleic Acids Res. *25*, 4666–4673. https://doi.org/10.1093/nar/25.22.4666.

Rohou, A., and Grigorieff, N. (2015). CTFFIND4: fast and accurate defocus estimation from electron micrographs. J. Struct. Biol. *192*, 216–221. https://doi.org/10.1016/j.jsb.2015.08.008.

Rossignol, J.L., and Faugeron, G. (1995). MIP: an epigenetic gene silencing process in Ascobolus immersus. Curr. Top. Microbiol. Immunol. *197*, 179–191. https://doi.org/10.1007/978-3-642-79145-1_12.

Roth, M., and Jeltsch, A. (2000). Biotin-avidin microplate assay for the quantitative analysis of enzymatic methylation of DNA by DNA methyltransferases. Biol. Chem. *381*, 269–272. https://doi.org/10.1515/BC.2000.035.

Scheres, S.H., and Chen, S. (2012). Prevention of overfitting in cryo-EM structure determination. Nat. Methods *9*, 853–854. https://doi.org/10.1038/nmeth.2115.

Song, J., Teplova, M., Ishibe-Murakami, S., and Patel, D.J. (2012). Structure-based mechanistic insights into DNMT1-mediated maintenance DNA methylation. Science *335*, 709–712. https://doi.org/10.1126/science.1214453.

Tollefsbol, T.O., and Hutchison, C.A., 3rd. (1997). Control of methylation spreading in synthetic DNA sequences by the murine DNA methyltransferase. J. Mol. Biol. *269*, 494–504. https://doi.org/10.1006/jmbi.1997.1064.

Turnbull, W.B., and Daranas, A.H. (2003). On the value of c: can low affinity systems be studied by isothermal titration calorimetry? J. Am. Chem. Soc. *125*, 14859–14866. https://doi.org/10.1021/ja036166s.

Unk, I., Hajdú, I., Blastyák, A., and Haracska, L. (2010). Role of yeast Rad5 and its human orthologs, HLTF and SHPRH in DNA damage tolerance. DNA Repair (Amst) *9*, 257–267. https://doi.org/10.1016/j.dnarep.2009.12.013.

Wang, Q., Yu, G., Ming, X., Xia, W., Xu, X., Zhang, Y., Zhang, W., Li, Y., Huang, C., Xie, H., et al. (2020). Imprecise DNMT1 activity coupled with neighbor-guided correction enables robust yet flexible epigenetic inheritance. Nat. Genet. *52*, 828–839. https://doi.org/10.1038/s41588-020-0661-y.

Willhoft, O., Ghoneim, M., Lin, C.L., Chua, E.Y.D., Wilkinson, M., Chaban, Y., Ayala, R., McCormack, E.A., Ocloo, L., Rueda, D.S., et al. (2018). Structure and dynamics of the yeast SWR1-nucleosome complex. Science *362*. https://doi.org/10.1126/science.aat7716.

Yan, L., Wu, H., Li, X., Gao, N., and Chen, Z. (2019). Structures of the ISWI-nucleosome complex reveal a conserved mechanism of chromatin remodeling. Nat. Struct. Mol. Biol. *26*, 258–266. https://doi.org/10.1038/s41594-019-0199-9.

Zheng, S.Q., Palovcak, E., Armache, J.P., Verba, K.A., Cheng, Y., and Agard, D.A. (2017). MotionCor2: anisotropic correction of beam-induced motion for improved cryo-electron microscopy. Nat. Methods *14*, 331–332. https://doi.org/10.1038/nmeth.4193.

Zivanov, J., Nakane, T., Forsberg, B.O., Kimanius, D., Hagen, W.J., Lindahl, E., and Scheres, S.H. (2018). New tools for automated high-resolution cryo-EM structure determination in RELION-3. eLife *7*, e42166. https://doi.org/10.7554/eLife.42166.

STAR★METHODS

KEY RESOURCES TABLE

REAGENT or RESOURCE	SOURCE	IDENTIFIER
Bacterial and virus strains		
E. coli BL21(DE3) competent cells	Novagen	Cat#69450-3
E. coli DH10Bac competent cells	Gibco	Cat#10361012
Chemicals, peptides, and recombinant proteins		
pFastBac HT B vector	Gibco	Cat#10584027
1M Tris-HCl pH8.0	Invitrogen	Cat#15568-025
Sodium Chloride	Fisher	Cat#S640-10
β-mercaptoethanol	Sigma-Aldrich	Cat#M6250-100ML
DTT	Gold Biotechnology	Cat#DTT100
5.0 M Magnesium chloride hexahydrate	Hampton	Cat#HR2-803
AMP-PNP	Sigma-Aldrich	Cat#10102547001
S-adenosyl-L-homocysteine (SAH)	Sigma-Aldrich	Cat#A9384-25MG
Protease inhibitor cocktail tablets, EDTA-free	Sigma-Aldrich	Cat#S8830-20TAB
S-adenosyl-L-methionine (SAM)	Millipore-Sigma	Cat# A4377
Mant-AMP-PNP	Biorbyt	Cat#orb63431 50 μl
Phenylmethanesulfonyl fluoride (PMSF)	Roche	Cat#11359061001
Sf-900 II SFM	Gibco	Cat#10-902-104
Grace's Insect Medium, supplemented	Gibco	Cat#11-605-094
Q5 site-directed mutagenesis kit	New England Biolabs	Cat#E0554S
Fetal bovine serum (FBS)	Gemini	Cat#900-108
Microplate, 384 well, PS, F-bottom, Black, Non-binding	Greiner Bio-one	Cat#781900
Microplate, 384 well, PS, F-bottom, Black, Med. binding	Greiner Bio-one	Cat#781076
Microplate, 96 well, PS, F-bottom, Clear	Greiner Bio-one	Cat#655101
S-[methyl-3 H]-adenosyl-L-methionine	Perkin Elmer	Cat# NET155H
ATP	Thermo Scientific	Cat#R1441
Benzonase nuclease	Millipore-Sigma	Cat# E1014
Ultima Gold	Perkin Elmer	Cat# 6013321
Critical commercial assays		
ADP-Glo Kinase Assay	Promega	Cat#V6930
ATPase/GTPase activity assay kit	Sigma-Aldrich	Cat#MAK113
Deposited data		
apo-DNMT5 coordinate	This paper	PDB: 7R76
apo-DNMT5 map	This paper	EMDB: EMD-24292
DNMT5 binary complex coordinate	This paper	PDB: 7R77
DNMT5 binary complex map	This paper	EMDB: EMD-24294
DNMT5 pseudo-ternary complex coordinate	This paper	PDB: 7T02
DNMT5 pseudo-ternary complex map	This paper	EMDB: EMD-25577
DNMT5 quaternary complex coordinate	This paper	PDB: 7R78
DNMT5 quaternary complex map	This paper	EMDB: EMD-24295
Experimental models: Cell lines		
insect cell *Spodoptera frugiperda* Sf9	Gibco	Cat#11496015
Trichoplusia ni High Five cells	Gibco	Cat#B85502

(*Continued on next page*)

Continued

REAGENT or RESOURCE	SOURCE	IDENTIFIER
Oligonucleotides		
hmDNA-F:CCATGCGCTGACACTAGA ATTGCCTAAGACCATACA	IDT	N/A
hmDNA-R:TGTATGGTCTTAGGCAAT TCTAGTGTCAG/iMedC/GCATGG, /iMedC/=5-methyl cytosine	IDT	N/A
umDNA-R:TGTATGGTCTTAGGCAAT TCTAGTGTCAGCGCATGG	IDT	N/A
FAM-hmDNA-F:/56-FAM/CCATGCGC TGACACTAGAATTGCCTAAG ACCA TACA	IDT	N/A
DNA_60bp_F: CATGGCCTAAGCCGGAC TGAATGAGCAAGCTTCCGGAGAATTCT GCCGGACTGCAGATGC	Dumesic et al., 2020	N/A
DNA_mCG_60bp_F: CATGGCCTAAGC/ iMedC/GGACTGAATGAGCAAGCTTC/ iMedC/GGAGAATTCTGC/iMedC/ GGACTGCAGATGC	Dumesic et al., 2020	N/A
Biot_DNA_60bp_Rev: 5Biosg/GCATCTGC AGTCCGGCAGAATTCTCCGGAAGCTTG CTCATTCAGTCCGGCTTAGGCCATG	This paper	N/A
Single_mCG_60bp_Fw: CATGGCCTAAG CaGGACTGAATGAGCAAGCTTC/iMe-dC/ GGAGAATTCTGCaGGACTGCAGATGC	Dumesic et al., 2020	N/A
Biot_SingleCG_60bp_Rev: 5Biosg/GCAT CTGCAGTCCtGCAGAATTCTCCGGAAGC TTGCTCATTCAGTCCtGCTTAGGCCATG	This paper	N/A
Recombinant DNA		
pFastBac-HTB-DNMT5	This paper	N/A
pFastBac-HTB-DNMT5 E637A	This paper	N/A
pFastBac-HTB-DNMT5 GS loop mutant	This paper	N/A
pFastBac-HTB-DNMT5 Q668A	This paper	N/A
pFastBac-HTB-DNMT5 R672A	This paper	N/A
pFastBac-HTB-DNMT5 R2036A	This paper	N/A
pFastBac-HTB-DNMT5 N447A	This paper	N/A
pFastBac-HTB-DNMT5 C684G	This paper	N/A
pFastBac-HTB-DNMT5 N669G/Q673A	This paper	N/A
Software and algorithms		
RELION-3	Zivanov et al., 2018	https://www3.mrc-lmb.cam.ac.uk/relion/; RRID: SCR_016274
Coot	Emsley et al., 2010	https://www2.mrc-lmb.cam.ac.uk/personal/pemsley/coot/; RRID: SCR_014222
UCSF Chimera	Pettersen et al., 2004	https://www.cgl.ucsf.edu/chimera/; RRID: SCR_004097
Phenix	Adams et al., 2010	https://phenix-online.org/; RRID: SCR_014224
Pymol	Schrodinger LLC	https://pymol.org/2/; RRID: SCR_000305
Prism 9	GraphPad	https://www.graphpad.com/; RRID: SCR_002798

(*Continued on next page*)

Continued

REAGENT or RESOURCE	SOURCE	IDENTIFIER
Origin 7	OriginLab	https://www.originlab.com/; RRID: SCR_002815
UCSF ChimeraX	Goddard et al., 2018	https://www.rbvi.ucsf.edu/chimerax/; RRID: SCR_015872
Other		
HisTrap FF (5 ml)	GE Healthcare	Cat#17-5255-01
HiTrap Q FF (5 ml)	GE Healthcare	Cat#17-5053-01
Superdex 200 increase 10/300 GL	GE Healthcare	Cat#28990944
Amicon concentrators (10K)	Millipore	Cat#UFC901024
Amicon concentrators (3K)	Millipore	Cat#UFC900308

RESOURCE AVAILABILITY

Lead contact

Further information and requests for resources and reagents should be directed to the lead contact Dinshaw J. Patel (pateld@mskcc.org).

Materials availability

All reagents generated in this study are available from the lead contact.

Data and code availability

The cryo-EM density maps and coordinate files for apo-DNMT5, the binary complex, the pseudo-ternary complex and the quaternary complex have been deposited in the EM Database and Protein Data Bank and are publicly available as of the date of publication. Accession numbers are listed in the key resources table.

- This paper does not report original code.
- Any additional information required to reanalyze the data reported in this paper is available from the lead contact upon request.

EXPERIMENTAL MODEL AND SUBJECT DETAILS

Bacterial cells

E. coli DH10Bac (Gibco) and BL21(DE3) were grown in LB at 37°C.

Insect cells

Expression of the DNMT5 wild-type and mutants were performed in *Trichoplusia ni* High Five cells (Gibco) that were cultured in the Sf-900 II SFM media (Gibco) at 27°C. Recombinant baculoviruses were generated using Bac-to-Bac baculovirus expression system according to manufacturer's instructions (Invitrogen). High titer baculoviruses were produced from adherent Sf9 cells cultured in Grace's insect medium, supplemented (Gibco) and 10% FBS (GEMINI) at 27°C.

METHOD DETAILS

Protein expression and purification

The gene encoding *C. neoformans* DNMT5 (residues 58–2377) was codon optimized and synthesized (Genewiz) for insect cell expression and inserted into pFastBac HT B vector (Gibco) with an N-terminal 6×His tag. Recombinant bacmid was generated in *E. coli* DH10Bac (Gibco) and then transfected into adherent *Spodoptera frugiperda* Sf9 cells (Gibco) for recombinant baculovirus packing. Supernatant containing the baculovirus was collected for reinfection and amplification. Suspension *Trichoplusia ni* High Five cells (Gibco) were infected by high titer baculovirus and collected after 72 h infection. The cells were disrupted by sonication in Binding buffer (20 mM Tris-HCl pH 8.0, 500 mM NaCl, 20 mM imidazole) supplemented with 1 mM PMSF (phenylmethylsulfonyl fluoride), 3 mM β-mercaptoethanol and protease inhibitor cocktail (Sigma-Aldrich). The recombinant DNMT5 was purified by 5 ml HisTrap Fastflow column (GE Healthcare) and dialyzed to low salt buffer (20 mM Tris, pH 8.0, 150 mM NaCl, 5 mM β-mercaptoethanol). The supernatant was further purified by HiTrap Q FF column and Superdex 200 increase 10/300 column (GE Healthcare). The pooled fractions were used for subsequent analysis or flash-frozen in liquid nitrogen.

DNMT5 mutations were generated using the Q5 site-directed mutagenesis kit (New England Biolabs) and verified by sequencing. All DNMT5 mutants were expressed and purified following the same protocol as the wild-type protein.

Cryo-EM sample preparation

For the DNMT5 apo form and binary complex, the purified DNMT5 was mixed with the 36-bp hmDNA, AMP-PNP, SAH at the molar ratio of 1:5:10:10 in the presence of 2 mM $MgCl_2$ and incubated on ice for 1 h. The mixture was further purified by gel filtration on the Superdex 200 increase 10/300 column (GE Healthcare) in buffer containing 20 mM Tris, pH 8.0, 150 mM NaCl, 2 mM DTT. The peak fractions containing DNMT5 complexes were pooled and concentrated at around 0.7 μM (OD_{280}~0.4, OD_{260}/OD_{280}=0.97) for cryo-EM grid preparation.

For the quaternary complex, the purified DNMT5 was diluted to the final concentration of ~0.2 mg/ml and incubated with the hmDNA, AMP-PNP and SAH at the molar ratio of 1:2:10:10 in buffer containing 20 mM Tris, pH 8.0, 150 mM NaCl, 2 mM DTT, 2 mM $MgCl_2$ for 1 h on ice. The mixture was subject to grid preparation directly without further purification.

The pseudo-ternary complex was prepared as for the quaternary complex except that SAH was changed to SAM and AMP-PNP was absent.

Cryo-EM data acquisition

3.5 μl peak fractions or incubated complexes were applied onto glow discharged UltrAuFoil 300 mesh R1.2/1.3 grids (Quantifoil) at ~4°C. Grids were blotted for 1.5 s at 100% humidity and flash frozen in liquid ethane using a Vitrobot Mark IV (FEI/Thermo Fisher Scientific). Images were collected on a Titan Krios G2 (FEI/Thermo Fisher Scientific) transmission electron microscope operating at 300 kV with a K3 direct detector (Gatan) using a 1.064 Å pixel size at the Memorial Sloan Kettering Cancer Center's Richard Rifkind Center for Cryo-EM. The defocus range was set from −1.0 to −2.5 μm. Movies were recorded in super-resolution mode at an electron dose rate of 20 e^-/ pixel/s with a total exposure time of 3 s and intermediate frames were recorded every 0.075 s for a total of 40 frames.

Image processing

For the DNMT5 apo form and binary complex dataset, stacks were motion corrected and 2× Fourier−cropped from a super-resolution pixel size of 0.532 Å using MotionCor2 (Zheng et al., 2017). Contrast transfer function parameters were estimated by CTFFIND-4 (Rohou and Grigorieff, 2015). Other steps of cryo-EM data processing were performed by RELION-3 (Zivanov et al., 2018). Particles were auto-picked without reference and extracted at a 3-fold binned pixel size of 3.192 Å. After two rounds of reference-free 2D classification, 715,061 particles were selected for 3D classification using an initial model as reference generated by RELION. 325,656 particles from the best two classes were refined, re-extracted to pixel size 1.064 Å and used for consensus 3D refinement. The resulting map had well-resolved density in the right segment and rather weak density in the left segment of DNMT5, indicating conformational heterogeneity. We tried to perform masked 3D classification on the left segment with the signal of the right segment subtracted from each raw particle image (Bai et al., 2015). The 325,656 density-subtracted particles were subject to 3D classification, while keeping all orientations fixed at the values determined in the consensus 3D refinement map. Classification into 8 classes yielded 2 major classes that showed good density (Figure S1A). The original and non-subtracted particles from the 2 good classes were used to perform 3D refinement separately. Postprocessing in RELION-3 (using pixel size 1.064 Å) yielded the final reconstructions at 3.1 Å for DNMT5 binary complex and 3.3 Å for apo-DNMT5.

The dataset of the quaternary complex was processed by a similar procedure as above. Briefly, 2,439,273 particles were auto-picked from 2,608 micrographs and 1,700,803 particles were selected for 3D classification after two rounds of reference-free 2D classification. After three rounds of 3D classification, 23,621 particles from the best class were subject to 3D refinement along with CTF refinement and particle polishing. The final reconstruction yielded the structure of the quaternary complex with an overall resolution of 3.5 Å.

For the DNMT5 pseudo-ternary complex dataset, 1,833,397 particles were auto-picked from 2,250 micrographs and 1,172,997 particles were selected for 3D classification after two rounds of reference-free 2D classification. After two rounds of 3D classification, 50,146 particles from the best class were subject to 3D refinement along with CTF refinement and particle polishing. The final reconstruction yielded the structure of the pseudo-ternary complex with an overall resolution of 3.7 Å.

All resolutions were estimated using RELION post-processing by applying a soft mask around the protein density and the Fourier shell correlation (FSC)=0.143 criterion (Scheres and Chen, 2012). The local resolution was calculated with RELION-3.

Atomic model building and refinement

The atomic model of the binary complex was *de novo* built manually in Coot (Emsley et al., 2010) based on the bulky amino acid side chains in the primary protein sequence. The apo-DNMT5, the quaternary complex and the pseudo-ternary complex models were built by docking the right and left segments of the binary complex model separately into the cryo-EM maps using UCSF Chimera (Pettersen et al., 2004) and then rebuilt and confirmed by bulky side chains in Coot. These models were refined by real-space refinement in Phenix (Adams et al., 2010) by applying geometric and secondary structure restraints. Structure figures were prepared with Pymol (pymol.org), UCSF Chimera and Chimera X (Goddard et al., 2018). Videos were prepared with UCSF Chimera.

Fluorescence polarization (FP) assay

DNMT5 or DNMT5-DNA mixture used for FP assays were serially diluted 2-fold in a buffer containing 20 mM Tris, pH 8.0, 50 mM NaCl, 2 mM $MgCl_2$, 2 mM DTT. The DNA binding FP assays were performed in non-binding, black flat-bottom 384-well plates (Greiner Bio-one) with the final assay volume of 20 μl per well. 6-carboxyfluorescein (FAM)-labeled double-stranded DNA (dsDNA) was generated by annealing equimolar amounts of sense and antisense oligonucleotides (IDT) using a PCR machine. Serially diluted DNMT5 were incubated with a final 50 nM concentration of FAM-labeled dsDNA at room temperature (RT) for 20 min. Polarizations were measured on a Tecan infinite m1000 microplate reader at an excitation wavelength of 470 nm and an emission wavelength of 520 nm. Scatter plots of polarizations versus DNMT5 concentration were plotted using Prism 9 (GraphPad) and dissociation constants (K_d) were fitted with the agonist vs. response variable slope (four parameters) model.

AMP-PNP competition FP assays were performed in medium binding, black flat-bottom 384-well plates (Greiner Bio-one) with the final assay volume of 20 μl per well. 1 μM DNMT5 was incubated with 100 nM FAM-labeled hmDNA or umDNA on ice for 1 hour. The 2x DNMT5-DNA mixtures were titrated with 2-fold serially diluted AMP-PNP at 1:1 volume ratio. Following a 20 min incubation period at RT, the polarizations were measured as above. The polarization values measured from wells containing DNMT5/FAM-dsDNA (in absence of AMP-PNP but same volume of buffer added) subtracting the values of only FAM-dsDNA (in absence of DNMT5) were normalized as 1. The normalized polarizations versus AMP-PNP concentration were plotted using Origin software.

For unlabeled umDNA and hmDNA competition FP assays, DNMT5 and FAM-labeled umDNA or hmDNA were incubated on ice for 30 min. AMP-PNP or equivalent volume of buffer were added to the mixture and incubated for another 30 min. Then increasing amounts of unlabeled umDNA or hmDNA were titrated to the samples at 1:1 volume ratio. The final concentrations are 0.5 μM for DNMT5, 50 nM for FAM-labeled umDNA or hmDNA and 2 μM for AMP-PNP. The polarization values measured from wells containing DNMT5/FAM-dsDNA (in absence of AMP-PNP but same volume of buffer added) subtracting the values measured from wells containing DNMT5/FAM-dsDNA (with AMP-PNP) competed by the highest concentration of unlabeled dsDNA (100 μM) were normalized as 1. The normalized polarizations versus unlabeled dsDNA concentration were plotted using Prism 9.

The ATP binding assays were performed in medium binding, black flat-bottom 384-well plates (Greiner Bio-one). DNMT5 was incubated with 4-fold molar excess hmDNA on ice for 1 hour and then 2-fold serially diluted. In the group without hmDNA, the same volume of buffer was added. 0.2 μM Fluorescent ATP analog 2'(3')-O-(N-methyl-anthraniloyl)-AMP-PNP (mantAMP-PNP) (Biorbyt) was mixed with serially diluted DNMT5 or DNMT5-hmDNA and incubated for 20 min at RT. Fluorescence polarization was measured on a SpectraMax M5 microplate reader (Molecular Devices LLC) with an excitation wavelength of 355 nm and an emission wavelength of 448 nm. The dissociation constants (K_d) were fitted in Prism 9 (GraphPad) with the agonist vs. response variable slope (four parameters) model.

Isothermal titration calorimetry (ITC)

Purified DNMT5 was incubated with 4-fold molar excess hmDNA or umDNA overnight on ice and 5-fold molar excess AMP-PNP or equivalent volume buffer were added to incubate on ice for another 1 h. The final concentration of DNMT5 is ~10 μM. SAH was dissolved to 200 μM in the same buffer as DNMT5 protein containing 20 mM Tris, pH 8.0, 50 mM NaCl, 2 mM $MgCl_2$, 5 mM β-mercaptoethanol. The titrations were performed on an iTC200 MicroCalorimeter (Malvern Panalytical) at 20°C with 300 rpm stirring speed. Each ITC titration consisted of 20 successive injections with 0.4 μl for the first injection and 2.0 μl for the rest. The resultant ITC curves were processed using Origin 7 software and fitted according to 'One Set of Sites' model with the stoichiometry (n value) fixed at 1 for valid curve fitting (Turnbull and Daranas, 2003).

ATPase assay

ATPase activity was assessed as described in (Catania et al., 2020). In brief, 30–60 nM of recombinant DNMT5 was incubated in ATPase reaction buffer (50 mM HEPES-KOH pH 7.9, 75 mM KCl, 5% Glycerol, 2 mM DTT, 2mM phosphoenolpyruvate (Sigma), 0.18 mM NADH (Sigma), 0.5 mM ATP, 5 mM $MgCl_2$, 10 U/ml pyruvate kinase (Sigma), 10 U/ml lactate dehydrogenase (Millipore). DNA substrates were added to a final concentration of 5 μM and the reactions performed at 25°C in a 384 well non-stick clear bottom plates (Corning 3766). The absorbance at 340 nm and 420 nm were measured using a Tecan Spark 10M. The difference between 340 nm and 420 nm was plotted versus time and the initial rate was calculated in the linear portion of the curve. The rate values were normalized over the concentration of DNMT5 used in the assay.

To measure ATPase activity in single turnover experiments (Figure S7), ADP produced from the reaction was measured using ADP-Glo Kinase assay (Promega) following the manual instructions. DNMT5 (1 μM) was incubated for 4 h in methyltransferase buffer + glucose (50 mM Tris-HCl pH 8, 25 mM NaCl, 10% Glycerol, 2mM DTT, 1 mM Glucose, 5 mM $MgCl_2$) in the presence of 0.5 mM ATP or AMP-PNP in a total volume of 5 μl. 5 μl of Reagent solution was added and incubated for 40 min at RT followed by addition of 10 μl of Detection solution and incubation for 60 min. The luminescence was detected using a Synergy H1 plate reader (BioTek). For some of the samples, a pre-incubation step with Hexokinase (36 U/ml, Sigma H-6380) was performed for 1 h at RT before addition of DNMT5. Free phosphate produced from the reaction was measured using ATPase/GTPase activity assay kit (Sigma) following the manual instructions. DNMT5 (1 μM) was incubated for 4 h with 100 nM hmDNA (possessing a single mCpG site), 1 mM ATP or AMP-PNP and 0.1 mM SAM at RT. The reaction mixtures were 20-fold diluted and 40 μl of the dilute solution was added to clear 96 well flat-bottom plate (Greiner Bio-one). Ultrapure water was included as background blank. Phosphate standards were serially diluted from 0 to 50 μM. 200 μl detection reagent was added to each well and incubated for an additional 30 min at

RT. The absorbance at 620 nm for standards, blanks and test wells were measured on a Tecan infinite m1000 microplate reader. The concentrations of free phosphate were calculated based on the fitted standard curve. The high-sensitivity kit can detect the free phosphate as low as 0.007 μM.

DNA methyltransferase assay

The DNA methyltransferase assays were carried out as described in (Roth and Jeltsch, 2000) with some modifications. DNMT5 (30 nM) was incubated at RT in methyltransferase buffer (50 mM Tris-HCl pH 8, 25 mM NaCl, 10% Glycerol, 2mM DTT, 1 mM ATP, 1 mM $MgCl_2$) in the presence of 5 μM biotinylated DNA substrate and 4 μM ^{3}H-SAM (PerkinElmer). 5 μl of reaction were removed at indicated time points and quenched in binding buffer (5 mM Tris-HCl pH 7.5, 0.5 mM EDTA, 1 M NaCl) containing 10 mM SAM in 10 mM H_2SO_4. At the end of the time course, the reactions were transferred to 96 well streptavidin-coated plates (Sigma- S2577) and incubated for 30 min at RT. The plates were washed 3 times in 200 μl of binding buffer and 3x 200 μl Digestion Buffer (50 mM Tris-HCl pH 8, 5 mM $MgCl_2$). To release the radioactivity incorporated in the DNA, the plates were incubated with 25U Benzonase Nuclease (Sigma) in 100 μl Digestion buffer for 1 h at RT. The reactions were then transferred in 3 ml of scintillation liquid (Ultima Gold-PerkinElmer) and the radioactivity detected on an LS 6500 scintillation counter (Beckman Coulter). Background signals (reaction without enzyme) were generally between 3 to 7 CPM. The initial rate values were calculated in the linear portion of the curve and normalized over the concentration of DNMT5. For the End point assays, the reactions were performed using the same protocol described above but in the presence of 100 nM DNMT5 and for 4 h.

Single turnover experiments were performed as described above but incubating 1 μM DNMT5 with 100 nM biotinylated hmDNA (possessing a single mCpG site) at RT and using 1 mM ATP or AMP-PNP.

QUANTIFICATION AND STATISTICAL ANALYSIS

The number of independent biological replicates for each assay is indicated in the corresponding figure legend. All quantitative data were presented as mean ± standard deviation (SD). Data were processed and plotted using Prism 9 and Origin 7 softwares. p values were calculated with Dunnett's test applied to a one-way ANOVA analysis using Prism 9. Statistical validations for the final structural models shown in Table 1 were performed in Phenix (Adams et al., 2010).